





Cite this: *Catal. Sci. Technol.*, 2023,  
13, 4744

# Role of polyoxometalate precursors and supports in the selective oxidation of methane into formaldehyde using supported metal oxide subnanocluster catalysts†

Keiju Wachi, Tomohiro Yabe, \* Takaaki Suzuki, Kentaro Yonesato,   
Kosuke Suzuki  and Kazuya Yamaguchi \*

The direct synthesis of useful chemicals from methane (CH<sub>4</sub>) is desirable; however, the products are prone to nonselective overoxidation, leading to the formation of CO<sub>2</sub>. A previous study developed a supported iron oxide subnanocluster catalyst with high thermal stability using iron-containing polyoxometalates (POMs) as precursors to selectively produce formaldehyde (HCHO) and CO. Herein, we investigated various supported POM-based catalysts to further improve the selectivity to HCHO *via* CH<sub>4</sub> oxidation, specifically by suppressing the pyrolysis and overoxidation of HCHO. After examining various metal-containing POM precursors and supports, we found that catalysts prepared using mononuclear- and dinuclear-iron-containing POM precursors supported on SiO<sub>2</sub> with a high specific surface area were effective and yielded relatively high quantities of HCHO. *In situ* diffuse reflectance infrared Fourier transform spectroscopy (DRIFTS) measurements under HCHO flow demonstrated that the pyrolysis and oxidation of HCHO were suppressed on SiO<sub>2</sub>, while the pyrolysis of HCHO was promoted on Al<sub>2</sub>O<sub>3</sub>. Furthermore, *in situ* DRIFTS measurements conducted at different temperatures revealed that HCHO was not decomposed or oxidized at 500 °C in the absence of catalysts.

Received 31st May 2023,  
Accepted 9th July 2023

DOI: 10.1039/d3cy00750b

rsc.li/catalysis

## Introduction

Methane (CH<sub>4</sub>), the main component of natural gas, is abundantly available worldwide, including in unconventional resources, such as biogas (including bio-methanation gas)<sup>1–3</sup> and CH<sub>4</sub> hydrates.<sup>4</sup> Furthermore, the production of carbon-neutral CH<sub>4</sub>, such as in power-to-gas technology, is expected to increase in the future. This production involves synthesizing CH<sub>4</sub> *via* methanation processes that utilize green hydrogen produced from renewable energy sources, such as water electrolysis and CO<sub>2</sub> emitted from power plants and factories.<sup>5–7</sup> Thus, CH<sub>4</sub> is gaining attention as a major energy resource and a promising chemical raw material.<sup>8–11</sup> However, CH<sub>4</sub>, with its tetrahedral shape and four identical C–H bonds, has the highest C–H bond energy (439 kJ mol<sup>−1</sup>) among sp<sup>3</sup>-hybridized hydrocarbons and is known as the least reactive alkane, making it very challenging to chemically convert into useful compounds.<sup>12</sup>

There are two methods for CH<sub>4</sub> conversion: indirect conversion *via* synthesis gas (syngas) and direct conversion to useful compounds, such as formaldehyde (HCHO), in one step.<sup>13</sup> Indirect conversion involves a syngas process, which is a high-temperature and high-pressure process that requires complicated and expensive equipment and significant energy consumption. Therefore, an economically viable direct conversion process of CH<sub>4</sub> into high-value-added chemicals is desired. One approach to economically achieve direct CH<sub>4</sub> conversion is to selectively oxidize CH<sub>4</sub> to oxygenates using O<sub>2</sub>. However, the target products are susceptible to thermal decomposition or sequential oxidation under the harsh oxidation conditions required for CH<sub>4</sub> activation. Therefore, developing a catalytic process that selectively synthesizes the desired products while suppressing sequential reactions is an urgent challenge for ensuring the stable supply of CH<sub>4</sub> oxidation-derived chemicals.

Catalysts for synthesizing HCHO from CH<sub>4</sub> have been developed since the 1980s, and various types of catalyst systems have been proposed, such as oxide catalysts,<sup>14,15</sup> supported catalysts,<sup>16–19</sup> and zeolite catalysts.<sup>20,21</sup> Commonly investigated oxide catalysts include molybdenum,<sup>16,17,19,22</sup> vanadium,<sup>16,23</sup> iron,<sup>24</sup> copper,<sup>22,25</sup> cobalt,<sup>21</sup> and tungsten.<sup>14,26</sup> However, bulk oxide and large nanoparticle catalysts have

Department of Applied Chemistry, School of Engineering, The University of Tokyo,  
7-3-1 Hongo, Bunkyo-ku, Tokyo 113-8656, Japan.

E-mail: tyabe@g.ecc.u-tokyo.ac.jp, kyama@appchem.t.u-tokyo.ac.jp

† Electronic supplementary information (ESI) available. See DOI: <https://doi.org/10.1039/d3cy00750b>

demonstrated relatively low selectivity to HCHO. For example, large nanoparticles of  $\text{VO}_x$  on the  $\text{VO}_x/\text{Al}_2\text{O}_3$  catalyst reduced both  $\text{CH}_4$  conversion and HCHO selectivity in  $\text{CH}_4$  oxidation.<sup>23</sup> Additionally, Zhang *et al.* reported that in molybdenum oxide catalysts,  $\text{CH}_4$  conversion and HCHO selectivity were related to the density of  $\text{Mo}=\text{O}$  bonds; namely,  $\text{Mo}=\text{O}$  bonds on  $\text{Zr}(\text{MoO}_4)_2$  were responsible for HCHO production, whereas excess lattice oxygen and bulk  $\text{MoO}_3$  caused overoxidation of HCHO.<sup>27</sup> In the case of iron oxide catalysts, isolated active lattice oxygen atoms on the surface of iron oxides helped to suppress overoxidation during  $\text{CH}_4$  oxidation.<sup>28</sup> Thus, supported metal oxide nanocluster catalysts have attracted attention, with reported examples including supported  $\text{CuO}_x$ ,<sup>29</sup>  $\text{FeO}_x$ ,<sup>30,31</sup>  $\text{MoO}_x$ ,<sup>32</sup> and  $\text{VO}_x$  nanocluster catalysts.<sup>33</sup>

The choice of catalyst supports is also significant in selective  $\text{CH}_4$  oxidation, and various oxide supports have been investigated, with  $\text{SiO}_2$  being recognized as the most suitable support. Kobayashi *et al.* discovered that highly dispersed  $\text{Fe}^{3+}$  species on  $\text{SiO}_2$  with isolated tetrahedrally coordinated Fe–O species significantly promoted selective HCHO production.<sup>34</sup> Although detailed mechanistic studies are still in progress, it is evident that highly dispersed active sites in  $\text{FeO}_x$  nanoclusters on  $\text{SiO}_2$  are essential for achieving selective HCHO production. Similarly, there is ongoing debate regarding the reaction mechanism of pyrolysis and overoxidation on  $\text{SiO}_2$  and other supports.

A polyoxometalate (POM) is an anionic metal oxide cluster consisting of metal–oxygen polyhedral units, such as  $\{\text{WO}_6\}$ .<sup>35,36</sup> The structure formed by eliminating some of the polyhedral units is called a lacunary POM, which functions as an inorganic multidentate ligand and allows the incorporation of different metals.<sup>37–39</sup> Recent studies have reported a new synthesis method for introducing various multinuclear

metal oxide clusters into lacunary POMs in organic solvents.<sup>40–44</sup> Furthermore, a previous study used a diiron-containing POM (**Fe2**) as a precursor to *in situ* form  $\text{FeO}_x$  subnanoclusters on  $\text{SiO}_2$ , which served as the active species to selectively convert  $\text{CH}_4$  into HCHO and  $\text{CO}$ .<sup>45</sup> This catalyst maintained the catalytic activity at 600 °C for 72 h, because the  $\text{FeO}_x$  subnanoclusters were dispersed in tungsten oxide species and inhibited from aggregation and deactivation. Another study successfully developed a method to achieve highly dispersed POM tetra-*n*-butylammonium (TBA) salts on various supports.<sup>46</sup> Therefore, using POMs with different multinuclear metal oxide cores as catalyst precursors allows the investigation of various highly stable metal oxide subnanoclusters for the selective conversion of  $\text{CH}_4$  to HCHO.

In this study, to further enhance the HCHO yield, we investigated  $\text{CH}_4$  oxidation by using various POMs supported on  $\text{SiO}_2$  as catalyst precursors (Fig. 1). Catalysts prepared using mononuclear (**Fe1**)- and dinuclear (**Fe2**)-iron-containing POM precursors supported on  $\text{SiO}_2$  produced relatively high yields of HCHO. Furthermore, we investigated  $\text{CH}_4$  oxidation using various supports. The results demonstrated that although  $\text{CH}_4$  conversion increased when using **Fe2**/ $\text{Al}_2\text{O}_3$  and **Fe2**/ $\text{CeO}_2$ , overoxidation to  $\text{CO}_2$  was promoted. We observed that catalysts prepared using  $\text{SiO}_2$  (*i.e.*, **Fe2**/ $\text{SiO}_2$ ) exhibited significantly higher HCHO yields than catalysts prepared using other supports. In addition, to elucidate the mechanism underlying the suppression of overoxidation of HCHO on **Fe2**/ $\text{SiO}_2$ , we investigated HCHO oxidation using  $\text{Al}_2\text{O}_3$  and  $\text{SiO}_2$  with different specific surface areas. We found that  $\text{SiO}_2$  suppressed HCHO pyrolysis, and the suppression was enhanced as the specific surface area of  $\text{SiO}_2$  increased. Moreover, we conducted temperature variation tests on HCHO oxidation and observed that HCHO was minimally decomposed or oxidized at 500 °C in the absence of catalysts.

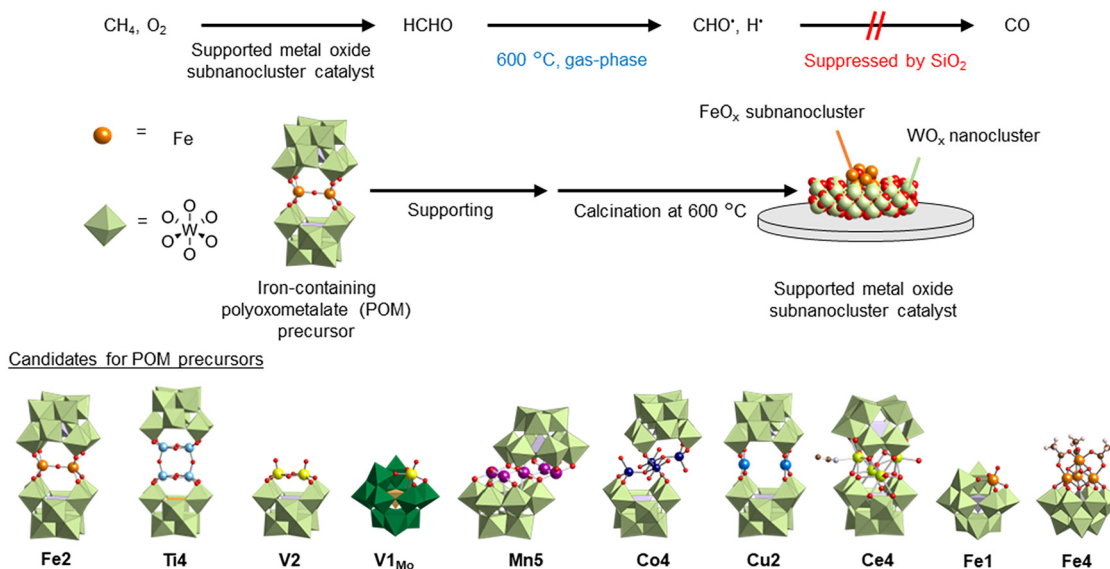


Fig. 1 Schematic diagram of the catalytic performance for  $\text{CH}_4$  oxidation using supported metal oxide subnanocluster catalyst prepared from polyoxometalates.

## Experimental

### Catalyst characterization

Cold-spray ionization (CSI)-mass spectra were recorded on a JEOL JMS-T100CS spectrometer. Infrared (IR) spectra were measured on a JASCO FT/IR-4100 spectrophotometer using KBr disks. Inductively coupled plasma atomic emission spectroscopy (ICP-AES) analysis was performed on a Shimadzu ICPS-8100 instrument. Brunauer–Emmett–Teller (BET) surface areas were measured by N<sub>2</sub> adsorption at −196 °C using a Micromeritics TriStar II Plus instrument. Raman spectra were recorded on a JASCO NRS-5100 spectrometer. The measurement conditions included an irradiation laser wavelength of 532 nm and a laser power of 10.2 mW, and the data were collected twice with a measurement time of 3 min. X-ray absorption spectroscopy (XAS) of the Fe K-edge was performed using the transmission and fluorescence method at the BL14B2 beamline of SPring-8 (proposal numbers 2022B1656 and 2023A1512). The X-ray beam was monochromatized using a Si (111) monochromator, and the energy was calibrated using an Fe metal foil for the Fe K-edge XAS. X-ray absorption near-edge structure (XANES) and extended X-ray absorption fine structure (EXAFS) data were analyzed using Athena and Artemis software (Demeter, version 0.9.26; Bruce Ravel). The *k*<sup>3</sup>-weighted EXAFS spectra were Fourier-transformed into *R*-space in the range of 3–12 Å<sup>−1</sup> for Fe. The XAS measurement methods and EXAFS analyses are explained in detail in the ESI.†

### Reagents

Dichloromethane, diethyl ether, and acetonitrile were purchased from Kanto Chemicals. SiO<sub>2</sub> (CARIACT Q-6, Q-10, Q-30, or Q-50, Fuji Silysia Chemical Ltd.), Al<sub>2</sub>O<sub>3</sub> (KHS-46, Sumitomo Chemical Co. Ltd.), ZrO<sub>2</sub> (JRC-ZRO-6, Daiichi Kigenso Kagaku Kogyo Co., Ltd), CeO<sub>2</sub> (JRC-CEO-5, Daiichi Kigenso Kagaku Kogyo Co., Ltd.), TiO<sub>2</sub> (ST-01, ISHIHARA SANGYO KAISHA, Ltd), Nb<sub>2</sub>O<sub>5</sub> (JRC-NBO-1, Companhia Brasileira de Metalurgia e Mineração), hydroxyapatite (HAP, Cat. No. 012-14882 FUJIFILM Wako Pure Chemical Corporation), and boron nitride (BN, Cat. No. 028-02281, FUJIFILM Wako Pure Chemical Corporation) were acquired from commercial sources. To represent SiO<sub>2</sub> with different specific surface areas, CARIACT Q-6, CARIACT Q-30, and CARIACT Q-50 are denoted as SiO<sub>2</sub>-Q6, SiO<sub>2</sub>-Q30, and SiO<sub>2</sub>-Q50, respectively. SiO<sub>2</sub> without any specific indication refers to CARIACT Q-10. Fe<sub>3</sub>O(CH<sub>3</sub>CO<sub>2</sub>)<sub>7</sub>(H<sub>2</sub>O)<sub>3</sub> (ref. 47) and TBA<sub>4</sub>[SiW<sub>9</sub>O<sub>28</sub>(OCH<sub>3</sub>)<sub>6</sub>]<sup>48,49</sup> were synthesized according to the reported procedures.

### Synthesis of various POMs

TBA<sub>8</sub>H<sub>4</sub>Fe<sub>2</sub>O(SiW<sub>10</sub>O<sub>36</sub>)<sub>2</sub> (**Fe2**),<sup>45</sup> TBA<sub>6</sub>Ti<sub>4</sub>O<sub>2</sub>(OH)<sub>4</sub>(PW<sub>10</sub>O<sub>36</sub>)<sub>2</sub> (**Ti4**),<sup>50</sup> TBA<sub>4</sub>V<sub>2</sub>O<sub>2</sub>(OH)<sub>2</sub>SiW<sub>10</sub>O<sub>36</sub> (**V2**),<sup>51</sup> TBA<sub>4</sub>VOPMo<sub>11</sub>O<sub>39</sub> (**V1Mo**),<sup>52</sup> TBA<sub>7</sub>HMn<sub>5</sub>(OH)<sub>2</sub>(SiW<sub>9</sub>O<sub>34</sub>)<sub>2</sub> (**Mn5**),<sup>42</sup> TBA<sub>8</sub>H<sub>4</sub>Co<sub>4</sub>(OH)<sub>4</sub>(SiW<sub>10</sub>O<sub>36</sub>)<sub>2</sub> (**Co4**),<sup>53</sup> TBA<sub>8</sub>H<sub>4</sub>Cu<sub>2</sub>(SiW<sub>10</sub>O<sub>36</sub>)<sub>2</sub> (**Cu2**),<sup>40</sup> TBA<sub>6</sub>Ce<sub>4</sub>(H<sub>2</sub>O)<sub>2</sub>(CH<sub>3</sub>CN)<sub>2</sub>O(SiW<sub>10</sub>O<sub>36</sub>)<sub>2</sub> (**Ce4**),<sup>41</sup> and TBA<sub>4</sub>HFe(H<sub>2</sub>O)SiW<sub>11</sub>O<sub>39</sub> (**Fe1**)<sup>54,55</sup> were synthesized according to the reported

procedures. In addition, TBA<sub>4</sub>Fe<sub>4</sub>(OH)<sub>3</sub>(CH<sub>3</sub>CO<sub>2</sub>)<sub>3</sub>SiW<sub>9</sub>O<sub>34</sub> (**Fe4**) was synthesized according to the following procedure. SiW<sub>9</sub>-OMe (500 mg, 152 μmol) was added to a dichloromethane solution (40 mL) of Fe<sub>3</sub>O(CH<sub>3</sub>CO<sub>2</sub>)<sub>7</sub>(H<sub>2</sub>O)<sub>3</sub> (134 mg, 205 μmol), and the resulting solution was stirred for 24 h at room temperature. Then, the remaining precipitate was filtered off, and the filtrate was dropped into diethyl ether (40 mL). Finally, the generated precipitate was collected by filtration through a membrane filter. After vacuum drying, a powder sample of **Fe4** was obtained. The anionic structure of **Fe4** was estimated from the IR spectra (Fig. S1†), ICP-AES elemental analysis, and CSI-mass spectrum (Fig. S2†), as described below. The IR spectra illustrated acetate peaks slightly shifted from those of Fe<sub>3</sub>O(CH<sub>3</sub>CO<sub>2</sub>)<sub>7</sub>(H<sub>2</sub>O)<sub>3</sub>. The elemental analysis confirmed that four Fe<sup>3+</sup> ions were introduced into an [SiW<sub>9</sub>O<sub>34</sub>]<sup>10−</sup> (**SiW9**) unit. The CSI-mass spectrum indicated the presence of a molecule containing four iron atoms, an **SiW9** unit, three hydroxide ligands, and three acetate ligands (Fig. S2†). These results suggested that **Fe4** had a cubane-type structure, as illustrated in Fig. 1, since a similar structure was reported for a manganese analogue according to the IR results.<sup>56</sup> IR (KBr pellet, cm<sup>−1</sup>): 3441, 2962, 2874, 1631, 1581, 1544, 1485, 1460, 1382, 1275, 1152, 1106, 1000, 958, 909, 804, 672, 524, 376, 359, 324, 319, 303, 297, 290, 282, 278, 271, 257, 252. Elemental analysis: calcd (%) for TBA<sub>4</sub>Fe<sub>4</sub>(OH)<sub>3</sub>(CH<sub>3</sub>CO<sub>2</sub>)<sub>3</sub>SiW<sub>9</sub>O<sub>34</sub>·2CH<sub>2</sub>Cl<sub>2</sub>, Si 0.74, Fe 5.85, W 43.33; found Si 0.74, Fe, 5.87, W 43.38. Positive-ion CSI-mass (acetonitrile): *m/z* = 3891.36, [TBA<sub>5</sub>Fe<sub>4</sub>(OH)<sub>3</sub>(CH<sub>3</sub>CO<sub>2</sub>)<sub>3</sub>SiW<sub>9</sub>O<sub>34</sub>]<sup>+</sup> (theoretical *m/z* = 3890.48).

### Preparation of POM-supported catalysts

Various types of POMs were generally dispersed on supports with the loading amount of 10 wt% using the incipient wetness method.<sup>46</sup> The preparation method of **Fe2**/SiO<sub>2</sub> is described as a typical example. A TBA salt of **Fe2** (100 mg) was dissolved in acetonitrile (2 mL). Then, the resulting solution was dropped onto a thin layer of SiO<sub>2</sub> (900 mg) spread on an evaporation tray. The resulting powder was dried at 100 °C for 5 h and then calcined at 600 °C for 5 h under air atmosphere, giving the **Fe2**/SiO<sub>2</sub> catalyst. Various kinds of supported catalysts were prepared by the same method using POM precursors shown in Fig. 1. These supported catalysts were denoted using the abbreviation of the POM precursors and supports, such as **Fe1**/SiO<sub>2</sub>, **Fe2**/SiO<sub>2</sub>, and **Fe4**/SiO<sub>2</sub>. As for **Fe2**/SiO<sub>2</sub>, the catalyst with 35 wt% **Fe2** (35**Fe2**/SiO<sub>2</sub>) was also prepared to align the loading amount of iron with **Fe4**/SiO<sub>2</sub>. Additionally, Cs-**Fe2**/SiO<sub>2</sub> was prepared following our previous report.<sup>46</sup> Briefly, TBA-**Fe2** was supported on SiO<sub>2</sub> in acetonitrile using the incipient wetness method. Then, Cs-**Fe2**/SiO<sub>2</sub> was obtained by cation exchange from TBA-**Fe2**/SiO<sub>2</sub> using cesium trifluoromethanesulfonate as the Cs source in ethanol.

### Evaluation of CH<sub>4</sub> and HCHO oxidation performance

Catalytic performance tests for CH<sub>4</sub> oxidation were conducted using a fixed-bed flow-type reactor schematically illustrated in Fig. S3a.† After 100 mg of catalyst was loaded into a quartz

tube reactor (6.0 mm i.d.), the reactant gas ( $\text{CH}_4:\text{O}_2:\text{Ar} = 2:1:7$ , total flow rate:  $50 \text{ mL min}^{-1}$ ) was introduced into the reactor. Then, the input temperature of the tube furnace containing the catalyst was increased to  $600 \text{ }^\circ\text{C}$  at a rate of  $10 \text{ }^\circ\text{C min}^{-1}$ . The inlet and outlet gases were heated to  $100 \text{ }^\circ\text{C}$  to reduce the temperature variation in the catalyst bed and to suppress the condensation of products. When the furnace temperature reached  $600 \text{ }^\circ\text{C}$ , it was maintained for 1 h to allow the activity to stabilize. Then, HCHO was trapped in 20 mL of an aqueous solution containing 2 g of  $\text{Na}_2\text{SO}_3$  and 50  $\mu\text{L}$  of  $\text{H}_2\text{SO}_4$ , and the amount of trapped HCHO was determined by titration with an aqueous solution of NaOH (0.1 M). CO and  $\text{CO}_2$  were analyzed immediately before and after HCHO collection using a Nexis GC-2030 gas chromatograph equipped with a barrier discharge ionization detector (Shimadzu Corporation) and a Shincarbon-ST packed column. The respective calculation formulas for  $\text{CH}_4$  conversion, product selectivity, and product yield in this study are as follows:

$$\text{CH}_4 \text{ conv. (\%)} = \frac{\text{Total carbon moles of HCHO, CO, and CO}_2}{\text{A carbon mole of input CH}_4} \times 100$$

$$\text{Product sel. (\%)} = \frac{\text{A carbon mole of HCHO, CO, or CO}_2}{\text{Total carbon moles of HCHO, CO, and CO}_2} \times 100$$

$$\text{Product yield (\%)} = \text{CH}_4 \text{ conv. (\%)} \times \text{Product sel. (\%)} \div 100$$

In the pyrolysis and oxidation test of HCHO, gaseous HCHO was generated by flowing Ar or  $\text{O}_2/\text{Ar}$  gas through 10 g of paraformaldehyde heated to  $55 \text{ }^\circ\text{C}$ , as illustrated in Fig. S3b.†

### *In situ* DRIFTS measurement

Diffuse reflectance infrared Fourier transform spectroscopy (DRIFTS) was performed using a JASCO FT/IR-6700 spectrometer equipped with an *in situ* sample cell in the range of  $1500\text{--}4000 \text{ cm}^{-1}$  at a resolution of  $4 \text{ cm}^{-1}$  (number of scans: 64). The samples were loaded onto a sample plate (6 mm diameter) and placed on the heater in the IR cell. The sample was pretreated by heating in a vacuum at  $600 \text{ }^\circ\text{C}$  for 1 h, and the background spectrum was measured. After the pretreatment, the sample was exposed to approximately 1% HCHO in  $\text{N}_2$  ( $20 \text{ mL min}^{-1}$ ) for 1 h. Then, the cell was evacuated into a vacuum at  $600 \text{ }^\circ\text{C}$ , and the DRIFTS spectra were measured both in the reactant gas and in a vacuum. HCHO was generated in the same manner as described above.

## Results and discussion

### $\text{CH}_4$ oxidation using various catalysts

First, the catalytic performance for  $\text{CH}_4$  oxidation was investigated for various POM-based catalysts at  $600 \text{ }^\circ\text{C}$  under atmo-

spheric pressure, and the results are presented in Table 1. **Ti4/SiO<sub>2</sub>**, **V2/SiO<sub>2</sub>**, **V1<sub>Mo</sub>/SiO<sub>2</sub>**, **Cu2/SiO<sub>2</sub>**, and **Ce4/SiO<sub>2</sub>** exhibited relatively low  $\text{CH}_4$  conversion (Table 1, entries 2–4, 7, and 8). Although there have been several reports<sup>16,17,19,22,23,25</sup> on the oxidation of  $\text{CH}_4$  to HCHO using vanadium, molybdenum, and copper oxides, the  $\text{CH}_4$  oxidation performance using these POM precursors supported on  $\text{SiO}_2$  was much lower than that using **Fe2/SiO<sub>2</sub>** (Table 1, entry 1). Particularly, the use of **Ce4/SiO<sub>2</sub>** resulted in minimal HCHO formation, with significant  $\text{CO}_2$  formation from complete  $\text{CH}_4$  oxidation (Table 1, entry 8). In contrast, although **Fe2/SiO<sub>2</sub>**, **Mn5/SiO<sub>2</sub>**, and **Co4/SiO<sub>2</sub>** exhibited relatively high  $\text{CH}_4$  conversion, the overoxidation to  $\text{CO}_x$  (CO and  $\text{CO}_2$ ) was more pronounced for **Mn5/SiO<sub>2</sub>** and **Co4/SiO<sub>2</sub>** than for **Fe2/SiO<sub>2</sub>** (Table 1, entries 1, 5, and 6). In the case of iron, reducing the cluster size promoted the partial oxidation of  $\text{CH}_4$  to HCHO, while the catalytic performance of manganese and cobalt nanoclusters remained similar to that of bulk oxides<sup>57</sup> or nanoparticles.<sup>58</sup> Thus, the catalytic performance for  $\text{CH}_4$  oxidation on  $\text{SiO}_2$ -supported metal oxide subnanocluster catalysts prepared from various POM precursors indicated that **Fe2/SiO<sub>2</sub>** catalysts exhibited the highest HCHO yield among the metal oxide subnanocluster catalysts with 3d metal or Ce metal multinuclear structures.

Next, the catalytic performance for  $\text{CH}_4$  oxidation was investigated for various Fe–POM-based catalysts prepared using iron-containing POM precursors with various multinuclear oxide cores at  $600 \text{ }^\circ\text{C}$  under atmospheric pressure. The results are summarized in Table 1. The iron content of the supported iron catalysts is also summarized in Table S1.† Among the catalysts prepared from POMs with different numbers of iron nuclei, **Fe1/SiO<sub>2</sub>** and **Fe2/SiO<sub>2</sub>** exhibited relatively high HCHO yields of 0.73% and 0.57%, respectively (Table 1, entries 1, 9, and 10). **Fe4/SiO<sub>2</sub>** exhibited a relatively high  $\text{CH}_4$  conversion of 3% but a low HCHO selectivity of 11%, resulting in a low HCHO yield of 0.33%. 35 wt% **Fe2/SiO<sub>2</sub>** (35**Fe2/SiO<sub>2</sub>**) was prepared using **Fe2** with the same iron loading amount as that of **Fe4/SiO<sub>2</sub>**, and the reaction was performed using 35**Fe2/SiO<sub>2</sub>**. As a result, 35**Fe2/SiO<sub>2</sub>** exhibited lower  $\text{CO}_2$  selectivity than **Fe4/SiO<sub>2</sub>** (Table 1, entries 10 and 11). In addition, Cs–**Fe2/SiO<sub>2</sub>** was prepared to improve the thermal stability of the anionic structure of **Fe2**,<sup>46</sup> and the  $\text{CH}_4$  oxidation performance of Cs–**Fe2/SiO<sub>2</sub>** was investigated under the same reaction conditions. However, despite its high selectivity toward HCHO (73%), Cs–**Fe2/SiO<sub>2</sub>** exhibited relatively low  $\text{CH}_4$  conversion (0.67%) (Table 1, entry 12).

To investigate the structural differences between **Fe2/SiO<sub>2</sub>**, 35**Fe2/SiO<sub>2</sub>** and **Fe4/SiO<sub>2</sub>** after the reaction, Fe K-edge XAFS measurements were performed, with the XANES and EXAFS spectra displayed in Fig. S4 and S5,† respectively. The Fe K-edge XANES results indicated that the valence of Fe in each catalyst prepared from **Fe2** and **Fe4** was not different. In a previous study, **Fe2/SiO<sub>2</sub>** was directly used for the reaction without any pretreatment.<sup>45</sup> In contrast, **Fe2/SiO<sub>2</sub>** in this study was used after calcination. The results of Fe K-edge XANES and EXAFS suggested that **Fe2/SiO<sub>2</sub>** prepared by

Table 1 Catalytic performance in CH<sub>4</sub> oxidation for various catalysts prepared from POM precursors<sup>a</sup>

Entry	Catalyst	Conv. [%]	Sel. [%]			Yield [%]
		CH <sub>4</sub>	HCHO	CO	CO <sub>2</sub>	HCHO
1	Fe2/SiO <sub>2</sub>	1.4	41	45	14	0.57
2	Ti4/SiO <sub>2</sub>	0.40	82	5	13	0.33
3	V2/SiO <sub>2</sub>	0.44	55	27	18	0.24
4	V1 <sub>Mo</sub> /SiO <sub>2</sub>	0.52	63	22	15	0.33
5	Mn5/SiO <sub>2</sub>	0.97	25	45	30	0.24
6	Co4/SiO <sub>2</sub>	1.4	22	52	26	0.30
7	Cu2/SiO <sub>2</sub>	0.69	47	27	26	0.33
8	Ce4/SiO <sub>2</sub>	0.56	—	66	34	—
9	Fe1/SiO <sub>2</sub>	1.4	54	32	13	0.73
10	Fe4/SiO <sub>2</sub>	3.0	11	62	28	0.33
11	35Fe2/SiO <sub>2</sub>	1.9	29	58	13	0.55
12	Cs-Fe2/SiO <sub>2</sub>	0.67	73	20	7	0.49

<sup>a</sup> Reaction conditions: 10 wt% supported catalyst (100 mg), CH<sub>4</sub>:O<sub>2</sub>:Ar = 2:1:7, 50 mL min<sup>-1</sup>, 1 atm, 600 °C.

calcination under air atmosphere formed a structure similar to that of Fe2/SiO<sub>2</sub> treated by the reaction gas (Fig. S4a, S5a and b†).<sup>45</sup> In our previous report on Fe2/SiO<sub>2</sub> (used for CH<sub>4</sub> oxidation without precalcination),<sup>45</sup> it was revealed that Fe2 was decomposed into FeO<sub>x</sub> subnanoclusters (<1 nm) and WO<sub>x</sub> nanoclusters (approximately 3 nm) on SiO<sub>2</sub> under CH<sub>4</sub> oxidation conditions at 600 °C. Various control experiments and characterizations also revealed that the FeO<sub>x</sub> subnanoclusters were the active species. Furthermore, the FeO<sub>x</sub> subnanoclusters were dispersed on the WO<sub>x</sub> nanoclusters, and as a result, excessive aggregation and deactivation of the effective FeO<sub>x</sub> subnanoclusters were suppressed. Thus, a similar structure was expected to form over Fe4/SiO<sub>2</sub>. The Fe K-edge XANES spectra of 35Fe2/SiO<sub>2</sub> and Fe4/SiO<sub>2</sub> suggested that they also had similar structures to the previously reported Fe2/SiO<sub>2</sub> (Fig. S4b†).<sup>45</sup> On the other hand, we found that the peak intensity corresponding to the Fe–O bond in the first coordination sphere for Fe2/SiO<sub>2</sub> and 35Fe2/SiO<sub>2</sub> was higher than that for Fe4/SiO<sub>2</sub> in the Fe K-edge EXAFS spectra (Fig. S5c and d†). This may be due to the larger number of WO<sub>x</sub> nanoclusters near the FeO<sub>x</sub> subnanoclusters in Fe2/SiO<sub>2</sub> and 35Fe2/SiO<sub>2</sub> than that in Fe4/SiO<sub>2</sub> since the amount of tungsten per iron in Fe2 was larger than that in Fe4. Furthermore, in the Raman spectrum of Fe2/SiO<sub>2</sub>, three main vibrational peaks were observed, corresponding to ν(W=O) at 980–960 cm<sup>-1</sup>, ν(W–O<sub>a</sub>–W) at 840–780 cm<sup>-1</sup>, and ν(W–O<sub>b</sub>–W) at 720–680 cm<sup>-1</sup> (Fig. S6†).<sup>59,60</sup> The terminal oxo species (W=O) corresponds to an isolated tungsten species. In contrast, in the spectrum of Fe4/SiO<sub>2</sub>, two peaks corresponding to ν(W–O<sub>a</sub>–W) and ν(W–O<sub>b</sub>–W) were observed and no ν(W=O) peak was observed. Considering that Fe2/SiO<sub>2</sub> and Fe4/SiO<sub>2</sub> contained almost the same amount of tungsten, 5.3 wt% and 4.5 wt%, respectively, there was a sufficient amount of WO<sub>x</sub> species near the FeO<sub>x</sub> subnanoclusters. The remaining WO<sub>x</sub> species on Fe2/SiO<sub>2</sub> formed the isolated tungsten species, possibly because the amount of tungsten per iron of Fe2 was larger than that of Fe4. Thus, these results were consistent with the EXAFS spectra (Fig. S5†). Therefore, the difference in the iron oxide subnanocluster structures formed

on SiO<sub>2</sub> was reflected in the catalytic performance. In addition, 35Fe2/SiO<sub>2</sub> exhibited higher HCHO selectivity than Fe4/SiO<sub>2</sub>, possibly due to the higher tungsten content and the presence of a larger number of tungsten oxide clusters, which inhibited the aggregation of FeO<sub>x</sub> subnanoclusters. In summary, the iron oxide subnanocluster catalysts prepared from Fe1 and Fe2 exhibited the highest HCHO yield in CH<sub>4</sub> oxidation.

### Support effect

The catalytic performance for CH<sub>4</sub> oxidation was investigated for Fe2-based catalysts prepared using various supports at 600 °C under atmospheric pressure. The results and specific surface areas of supported are summarized in Table 2. The results indicated that higher specific surface areas of SiO<sub>2</sub> supports resulted in higher CH<sub>4</sub> conversion (Table 2, entries 1–4). This suggested that a higher dispersion state of the Fe2 precursor on SiO<sub>2</sub> led to the generation of more dispersed iron oxide nanoclusters, resulting in increased CH<sub>4</sub> conversion and HCHO yield. The supported Fe2 catalyst prepared using SiO<sub>2</sub>-Q6, which had a very high specific surface area of 386 m<sup>2</sup> g<sup>-1</sup>, exhibited the highest CH<sub>4</sub> conversion and HCHO yield of 2.0% and 0.73%, respectively. In contrast, despite having lower specific surface areas than SiO<sub>2</sub>, the supported Fe2 catalysts prepared using Al<sub>2</sub>O<sub>3</sub>, ZrO<sub>2</sub>, and CeO<sub>2</sub> exhibited higher CH<sub>4</sub> conversion, resulting in the production of only CO<sub>x</sub> (Table 2, entries 5–7). In addition, the reaction was performed at 500 °C with Fe2/CeO<sub>2</sub>, but the selectivity to HCHO did not increase, although the CH<sub>4</sub> conversion decreased (Table 2, entry 8). Similar catalytic performance has been reported for FePO<sub>4</sub> catalysts supported on Al<sub>2</sub>O<sub>3</sub>, SiO<sub>2</sub>, TiO<sub>2</sub>, and ZrO<sub>2</sub>, suggesting that the choice of support affects the overoxidation of HCHO.<sup>18</sup>

The surface acidity of these supports may promote the easy activation of CH<sub>4</sub>, resulting in overoxidation of the products.<sup>61</sup> In addition, HAP, BN, Nb<sub>2</sub>O<sub>5</sub>, and TiO<sub>2</sub> had smaller specific surface areas than SiO<sub>2</sub>, resulting in lower CH<sub>4</sub> conversion when used as supports for Fe2 catalysts (Table 2,

Table 2 Catalytic performance over supported Fe2 catalysts on various supports<sup>a</sup>

Entry	Support	BET surface area [m <sup>2</sup> g <sup>-1</sup> ]	Conv. [%]		Sel. [%]		Yield [%]
			CH <sub>4</sub>	HCHO	CO	CO <sub>2</sub>	HCHO
1	SiO <sub>2</sub> -Q50	67	0.71	57	35	8	0.41
2	SiO <sub>2</sub> -Q30	100	0.96	43	44	13	0.42
3	SiO <sub>2</sub>	278	1.4	41	45	14	0.57
4	SiO <sub>2</sub> -Q6	386	2.0	36	46	18	0.73
5	Al <sub>2</sub> O <sub>3</sub>	158	6.1	—	82	18	—
6	ZrO <sub>2</sub>	40	3.3	—	78	22	—
7	CeO <sub>2</sub>	43	6.8	—	65	35	—
8	CeO <sub>2</sub> <sup>b</sup>	43	0.79	—	69	31	—
9	Nb <sub>2</sub> O <sub>5</sub>	145	0.84	39	51	10	0.33
10	TiO <sub>2</sub>	72	1.2	7	64	29	0.08
11	BN	6	0.28	57	24	19	0.16
12	HAP	9	0.12	67	n.d.	33	0.08

<sup>a</sup> Reaction conditions: supported Fe<sub>2</sub> catalyst (100 mg), CH<sub>4</sub>:O<sub>2</sub>:Ar = 2:1:7, 50 mL min<sup>-1</sup>, 1 atm, 600 °C. <sup>b</sup> 500 °C.

entries 9–12). Therefore, the effect of the support on CH<sub>4</sub> oxidation was found to depend on the type of support and its specific surface area. Moreover, it was found that the Fe<sub>2</sub> catalyst supported on SiO<sub>2</sub>, which was inert and had a high specific surface area, exhibited the highest HCHO yield.

### Pyrolysis and oxidation tests of HCHO

As the support significantly affected the overoxidation of HCHO, pyrolysis and oxidation tests of HCHO on various supports and Fe<sub>2</sub>/SiO<sub>2</sub> were investigated (Fig. 2). The results indicated that HCHO was decomposed by 80% or more even in the absence of catalysts at 600 °C (Fig. 2, entry 1). We found that HCHO pyrolysis was significantly suppressed in the presence of SiO<sub>2</sub> (Fig. 2, entry 2), and this suppression increased with the specific surface area of SiO<sub>2</sub> (Fig. 2, entry 3). Additionally, HCHO pyrolysis was suppressed by using Fe<sub>2</sub>/SiO<sub>2</sub> (Fig. 2, entry 4). In contrast, HCHO pyrolysis on Al<sub>2</sub>O<sub>3</sub> was promoted (Fig. 2, entry 5). HCHO overoxidation on SiO<sub>2</sub>

was more suppressed even in the presence of O<sub>2</sub> than in the absence of catalysts (Fig. 2, entries 6 and 7). Furthermore, HCHO conversion using Fe<sub>2</sub>/SiO<sub>2</sub> was lower than that in the absence of catalysts (Fig. 2, entry 8). These findings suggested that the reason for the high HCHO yield when using Fe<sub>2</sub>/SiO<sub>2</sub> was the suppression of HCHO pyrolysis by SiO<sub>2</sub> and the use of Fe<sub>2</sub> as a catalyst precursor. Meanwhile, even with an inert support such as SiO<sub>2</sub>, HCHO was sequentially oxidized in the presence of O<sub>2</sub> at 600 °C. Since a significant amount of HCHO was thermally decomposed even at 600 °C, pyrolysis and oxidation tests without catalysts were conducted at various temperatures, as illustrated in Fig. 3. The results indicated that both pyrolysis and oxidation were suppressed at lower temperatures and that almost no pyrolysis or oxidation occurred at 500 °C. In our previous study, however, the CH<sub>4</sub> conversion over Fe<sub>2</sub>/SiO<sub>2</sub> at 550 °C was lower than 1%, and the CH<sub>4</sub> conversion at 500 °C predicted based on the Arrhenius plots was below 0.4%.<sup>45</sup> Therefore, FeO<sub>x</sub> subnanocluster active site should be modified and improved to archive higher HCHO yield at 500 °C.

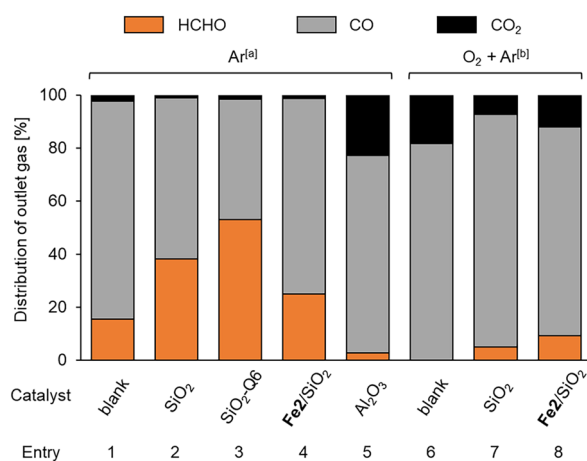
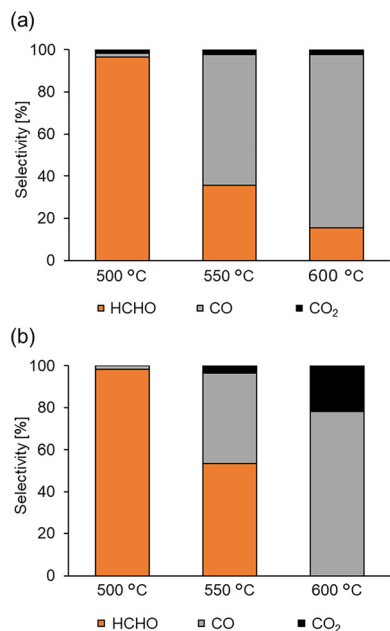


Fig. 2 HCHO pyrolysis and oxidation tests on various supports and Fe<sub>2</sub>/SiO<sub>2</sub>. Reaction conditions: catalyst (100 mg), HCHO (1%), 1 atm, 600 °C. [a] Ar (50 mL min<sup>-1</sup>), [b] O<sub>2</sub> (5 mL min<sup>-1</sup>), Ar (45 mL min<sup>-1</sup>).

### Proposed mechanism of the suppression of HCHO pyrolysis

To elucidate the mechanism by which pyrolysis of HCHO was promoted on Al<sub>2</sub>O<sub>3</sub> and suppressed on SiO<sub>2</sub>, *in situ* DRIFTS measurements were conducted at 600 °C. The DRIFTS spectra measured 60 min after evacuation following HCHO flow were presented in Fig. 4. The observed peaks of DRIFTS spectra and their assignments are summarized in Table S2.<sup>†</sup> Furthermore, time variation of *in situ* DRIFTS spectra of Al<sub>2</sub>O<sub>3</sub> and SiO<sub>2</sub> at 600 °C is illustrated in Fig. S7.<sup>†</sup> In the spectrum of Al<sub>2</sub>O<sub>3</sub>, three peaks observed at 1572, 2906, and 2997 cm<sup>-1</sup> were attributed to formate species (Fig. 4a). In addition, the peaks at 1630 and 3751 cm<sup>-1</sup> were attributed to H<sub>2</sub>O and an aluminol group, respectively, indicating that these species possibly involved in the mechanism.

On the other hand, in the spectrum of SiO<sub>2</sub>, two sharp peaks at 2959 and 2858 cm<sup>-1</sup> were observed (Fig. 4b). From the previously reported data summarized in Table. S2,<sup>†</sup> these



**Fig. 3** Pyrolysis and oxidation tests without catalysts at various temperatures. Reaction conditions: no catalyst, 1 atm, HCHO (ca. 0.6%). (a) Ar (50 mL min<sup>-1</sup>), (b) O<sub>2</sub> (5 mL min<sup>-1</sup>), Ar (45 mL min<sup>-1</sup>).

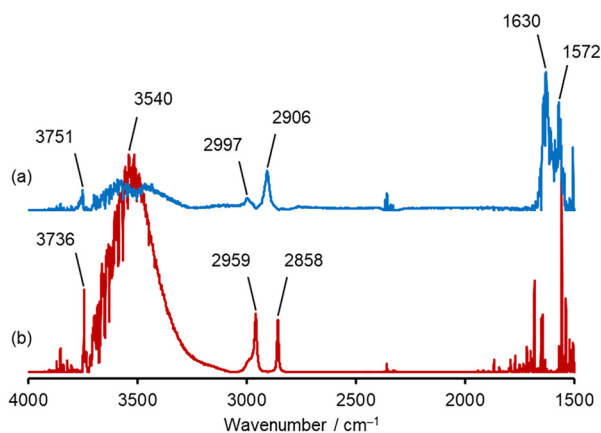


**Fig. 4** *In situ* DRIFTS spectra on (a) Al<sub>2</sub>O<sub>3</sub> and (b) SiO<sub>2</sub>. Analysis conditions: HCHO/N<sub>2</sub> mixture gas (20 mL min<sup>-1</sup>) flowed at 600 °C for 60 min. Then, the cell was evacuated, and DRIFTS spectra were measured 60 min later. The absorbance intensity on the vertical axis was Kubelka-Munk-transformed.

peaks can be attributed to dioxymethylene species. As well as Al<sub>2</sub>O<sub>3</sub>, the peaks derived from adsorbed H<sub>2</sub>O (ref. 65) at 3540 cm<sup>-1</sup> and a silanol group<sup>66</sup> at 3736 cm<sup>-1</sup> were observed. These findings suggested that the adsorbed HCHO was decomposed into formate on Al<sub>2</sub>O<sub>3</sub>, while not on SiO<sub>2</sub>.

We proposed a surface reaction mechanism of HCHO on Al<sub>2</sub>O<sub>3</sub> and SiO<sub>2</sub> based on the results of *in situ* DRIFTS, as displayed in Fig. 5. In the gas phase, CO is generated by HCHO pyrolysis *via* the formyl radical.<sup>67</sup> In the presence of Al<sub>2</sub>O<sub>3</sub>, HCHO reacts with aluminol groups on the surface to form dioxymethylene species. Then, the dioxymethylene spe-

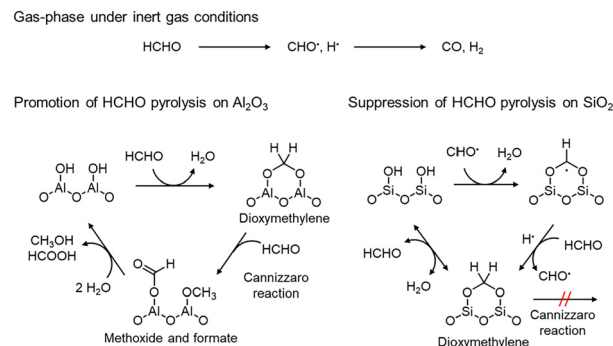


**Fig. 5** Proposed mechanism of the suppression of HCHO pyrolysis on SiO<sub>2</sub> and the promotion of HCHO pyrolysis on Al<sub>2</sub>O<sub>3</sub>.

cies reacts with another HCHO to afford formate and methoxide species *via* the Cannizzaro reaction.<sup>62</sup> Then, these species further react with H<sub>2</sub>O to form formic acid and methanol; however, due to the high temperature of 600 °C, they are possibly sequentially oxidized to CO<sub>x</sub>. Therefore, Al<sub>2</sub>O<sub>3</sub> undesirably promotes the overoxidation of HCHO to CO<sub>x</sub>.

In contrast, the dioxymethylene species adsorbed on SiO<sub>2</sub> do not cause the Cannizzaro reaction because SiO<sub>2</sub> possesses no strong acidic or basic sites. Moreover, the formyl radical reacts with silanol species, and adsorbed on SiO<sub>2</sub>. Then, the adsorbed radical species reacts with hydrogen atom or accepts hydrogen atom from HCHO to form dioxymethylene. Since the adsorbed dioxymethylene species reacts with H<sub>2</sub>O to generate HCHO, we consider that HCHO pyrolysis can be suppressed on SiO<sub>2</sub>. SiO<sub>2</sub>-Q6 suppressed HCHO pyrolysis more than SiO<sub>2</sub> possibly because SiO<sub>2</sub>-Q6 possessed more silanol groups to react with formyl radicals due to higher specific surface area.

## Conclusions

The catalytic performance for CH<sub>4</sub> oxidation using SiO<sub>2</sub>-supported metal oxide subnanocluster catalysts prepared from various POM precursors indicated that Fe1/SiO<sub>2</sub> and Fe2/SiO<sub>2</sub> exhibited the highest HCHO yields among oxide subnanocluster catalysts with 3d metal or Ce metal multinuclear oxide cores. In addition, we found that Fe2-based catalysts prepared using SiO<sub>2</sub> with a high specific surface area improved both the CH<sub>4</sub> conversion and HCHO yield. Pyrolysis and oxidation tests of HCHO on various supports revealed that HCHO was almost completely decomposed even in the absence of catalysts at 600 °C. Moreover, the pyrolysis and overoxidation of HCHO were suppressed when SiO<sub>2</sub> was used as the support. *In situ* DRIFTS measurement under HCHO flow demonstrated that the pyrolysis and oxidation of HCHO were suppressed on SiO<sub>2</sub>, while the pyrolysis of HCHO was promoted on Al<sub>2</sub>O<sub>3</sub>. Thus, to achieve even higher HCHO yields in the future, it is necessary to suppress the pyrolysis and oxidation of HCHO in the gas phase. As pyrolysis and oxidation did not occur below 500 °C in the absence of catalysts, it is necessary to develop more effective catalysts that can lower the temperature of CH<sub>4</sub> activation.

## Conflicts of interest

There are no conflicts to declare.

## Acknowledgements

This work was financially supported by JSPS KAKENHI Grant Number 22K14539, 22H04971 and JST CREST Grant Number JPMJCR17P4. We greatly appreciate Dr. Hironori Ofuchi (Japan Synchrotron Radiation Research Institute, SPring-8) for the support of XAFS measurements at BL14B2, Proposal Number 2022B1656 and 2023A1512.

## Notes and references

- 1 D. Sutton, B. Kelleher and J. R. H. Ross, *Fuel Process. Technol.*, 2001, **73**, 155–173.
- 2 J. Kopyscinski, T. J. Schildhauer and S. M. A. Biollaz, *Fuel*, 2010, **89**, 1763–1783.
- 3 G. Strobel, B. Hagemann, T. M. Huppertz and L. Ganzer, *Renewable Sustainable Energy Rev.*, 2020, **123**, 109747.
- 4 J. Kondori, S. Zendejboudi and L. James, *Fuel*, 2019, **249**, 264–276.
- 5 F. M. Mota and D. H. Kim, *Chem. Soc. Rev.*, 2019, **48**, 205–259.
- 6 M. Held, D. Schollenberger, S. Sauerschell, S. Bajohr and T. Kolb, *Chem. Ing. Tech.*, 2020, **92**, 595–602.
- 7 A. Giocoli, V. Motola, N. Scarlat, N. Pierro and S. Dipinto, *Renewable Sustainable Energy Transition*, 2023, **3**, 100051.
- 8 M. C. Alvarez-Galvan, N. Mota, M. Ojeda, S. Rojas, R. M. Navarro and J. L. G. Fierro, *Catal. Today*, 2011, **171**, 15–23.
- 9 C. Hammond, S. Conrad and I. Hermans, *ChemSusChem*, 2012, **5**, 1668–1686.
- 10 P. Schwach, X. Pan and X. Bao, *Chem. Rev.*, 2017, **117**, 8497–8520.
- 11 N. F. Dummer, D. J. Willock, Q. He, M. J. Howard, R. J. Lewis, G. Qi, S. H. Taylor, J. Xu, D. Bethell, C. J. Kiely and G. J. Hutchings, *Chem. Rev.*, 2023, **123**, 6359–6411.
- 12 T. J. Hall, J. S. J. Hargreaves, G. J. Hutchings, R. W. Joyner and S. H. Taylor, *Fuel Process. Technol.*, 1995, **42**, 151–178.
- 13 J. H. Lunsford, *Catal. Today*, 2000, **63**, 165–174.
- 14 K. Otsuka and M. Hatano, *J. Catal.*, 1987, **108**, 252–255.
- 15 E. M. Coda, E. Mulhall, R. van Hoek and B. K. Hodnett, *Catal. Today*, 1989, **4**, 383–387.
- 16 A. Parmaliana and F. Arena, *J. Catal.*, 1997, **167**, 57–65.
- 17 K. Aoki, M. Ohmae, T. Nanba, K. Takeishi, N. Azuma, A. Ueno, H. Ohfuné, H. Hayashi and Y. Udagawa, *Catal. Today*, 1998, **45**, 29–33.
- 18 R. L. McCormick and G. O. Alptekin, *Catal. Today*, 2000, **55**, 269–280.
- 19 N. Ohler and A. T. Bell, *J. Phys. Chem. B*, 2006, **110**, 2700–2709.
- 20 A. de Lucas, J. L. Valverde, L. Rodriguez, P. Sanchez and M. T. Garcia, *Appl. Catal., A*, 2000, **203**, 81–90.
- 21 N. V. Beznis, A. N. C. van Laak, B. M. Weckhuysen and J. H. Bitter, *Microporous Mesoporous Mater.*, 2011, **138**, 176–183.
- 22 T. Akiyama, R. Sei and S. Takenaka, *Catal. Sci. Technol.*, 2021, **11**, 5273–5281.
- 23 S. Pei, B. Yue, L. Qian, S. Yan, J. Cheng, Y. Zhou, S. Xie and H. He, *Appl. Catal., A*, 2007, **329**, 148–155.
- 24 A. Matsuda, H. Tateno, K. Kamata and M. Hara, *Catal. Sci. Technol.*, 2021, **11**, 6987–6998.
- 25 T. Akiyama, M. Shimakawa and S. Takenaka, *Chem. Lett.*, 2022, **51**, 511–514.
- 26 A. de Lucas, J. L. Valverde, P. Cañizares and L. Rodriguez, *Appl. Catal., A*, 1999, **184**, 143–152.
- 27 Q. Zhang, W. Yang, X. Wang, Y. Wang, T. Shishido and K. Takehira, *Microporous Mesoporous Mater.*, 2005, **77**, 223–234.
- 28 F. Arena, G. Gatti, G. Martra, S. Coluccia, L. Stievano, L. Spadaro, P. Famulari and A. Parmaliana, *J. Catal.*, 2005, **231**, 365–380.
- 29 Y. Li, D. An, Q. Zhang and Y. Wang, *J. Phys. Chem. C*, 2008, **112**, 13700–13708.
- 30 Q. Zhang, Y. Li, D. An and Y. Wang, *Appl. Catal., A*, 2009, **356**, 103–111.
- 31 J. He, Y. Li, D. An, Q. Zhang and Y. Wang, *J. Nat. Gas Chem.*, 2009, **18**, 288–294.
- 32 Y. Kim, T. Y. Kim, C. K. Song, K. R. Lee, S. Bae, H. Park, D. Yun, Y. S. Yun, I. Nam, J. Park, H. Lee and J. Yi, *Nano Energy*, 2021, **82**, 105704.
- 33 H. Berndt, A. Martin, A. Brückner, E. Schreier, D. Müller, H. Kosslick, G.-U. Wolf and B. Lücke, *J. Catal.*, 2000, **191**, 384–400.
- 34 T. Kobayashi, N. Guilhaume, J. Miki, N. Kitamura and M. Haruta, *Catal. Today*, 1996, **32**, 171–175.
- 35 M. Sun, J. Zhang, P. Putaj, V. Caps, F. Lefebvre, J. Pelletier and J.-M. Basset, *Chem. Rev.*, 2014, **114**, 981–1019.
- 36 S.-S. Wang and G.-Y. Yang, *Chem. Rev.*, 2015, **115**, 4893–4962.
- 37 P. Putaj and F. Lefebvre, *Coord. Chem. Rev.*, 2011, **255**, 1642–1685.
- 38 D.-L. Long, R. Tsunashima and L. Cronin, *Angew. Chem., Int. Ed.*, 2010, **49**, 1736–1758.
- 39 A. Tézé, G. Hervé, R. G. Finke and D. K. Lyon, *Inorg. Synth.*, 1990, **27**, 85–96.
- 40 K. Suzuki, M. Shinoue and N. Mizuno, *Inorg. Chem.*, 2012, **51**, 11574–11581.
- 41 K. Suzuki, F. Tang, Y. Kikukawa, K. Yamaguchi and N. Mizuno, *Angew. Chem., Int. Ed.*, 2014, **53**, 5356–5360.
- 42 K. Suzuki, R. Sato, T. Minato, M. Shinoue, K. Yamaguchi and N. Mizuno, *Dalton Trans.*, 2015, **44**, 14220–14226.
- 43 Y. Sunada, K. Yamaguchi and K. Suzuki, *Coord. Chem. Rev.*, 2022, **469**, 214673.
- 44 Y. Koizumi, K. Yonesato, K. Yamaguchi and K. Suzuki, *Inorg. Chem.*, 2022, **61**, 9841–9848.
- 45 K. Wachi, T. Yabe, T. Suzuki, K. Yonesato, K. Suzuki and K. Yamaguchi, *Appl. Catal., B*, 2022, **314**, 121420.
- 46 T. Suzuki, T. Yabe, K. Wachi, K. Yonesato, K. Suzuki and K. Yamaguchi, *ChemNanoMat*, 2023, **9**, e202200428.
- 47 A. K. Pandey, T. Gupta and B. P. Baranwal, *Transition Met. Chem.*, 2004, **29**, 370–375.

- 48 T. Minato, K. Suzuki, K. Kamata and N. Mizuno, *Chem. – Eur. J.*, 2014, **20**, 5946–5952.
- 49 T. Minato, K. Suzuki, K. Yamaguchi and N. Mizuno, *Chem. – Eur. J.*, 2017, **23**, 14213–14220.
- 50 E. Takahashi, K. Kamata, Y. Kikukawa, S. Sato, K. Suzuki, K. Yamaguchi and N. Mizuno, *Catal. Sci. Technol.*, 2015, **5**, 4778–4789.
- 51 N. Nakagawa, K. Uehara and N. Mizuno, *Inorg. Chem.*, 2005, **44**, 9068–9075.
- 52 K. Nomiyama, K. Yagishita, Y. Nemoto and T. Kamataki, *J. Mol. Catal. A: Chem.*, 1997, **126**, 43–53.
- 53 Y. Kuriyama, Y. Kikukawa, K. Suzuki, K. Yamaguchi and N. Mizuno, *Chem. – Eur. J.*, 2016, **22**, 3962–3966.
- 54 M. S. Balula, J. A. Gamelas, H. M. Carapuça, A. M. V. Cavaleiro and W. Schlindwein, *Eur. J. Inorg. Chem.*, 2004, **2004**, 619–628.
- 55 F. Zonnevijlle, C. M. Tourne and G. F. Tourne, *Inorg. Chem.*, 1982, **21**, 2751–2757.
- 56 R. Al-Oweini, B. S. Bassil, J. Friedl, V. Kottisch, M. Ibrahim, M. Asano, B. Keita, G. Novitchi, Y. Lan, A. Powell, U. Stimming and U. Kortz, *Inorg. Chem.*, 2014, **53**, 5663–5673.
- 57 Y.-F. Han, L. Chen, K. Ramesh, Z. Zhong, F. Chen, J. Chin and H. Mook, *Catal. Today*, 2008, **131**, 35–41.
- 58 H. Wang, C. Chen, Y. Zhang, L. Peng, S. Ma, T. Yang, H. Guo, Z. Zhang, D. S. Su and J. Zhang, *Nat. Commun.*, 2015, **6**, 7181.
- 59 E. I. Ross-Medgaarden and I. E. Wachs, *J. Phys. Chem. C*, 2007, **11**, 15089–15099.
- 60 S. Chen, L. Zeng, H. Tian, X. Li and J. Gong, *ACS Catal.*, 2017, **7**, 3548–3559.
- 61 W. H. Cheng, *J. Catal.*, 1996, **158**, 477–485.
- 62 G. Busca, J. Lamotte, J.-C. Lavalley and V. Lorenzelli, *J. Am. Chem. Soc.*, 1987, **109**, 5197–5202.
- 63 D. B. Clarke, D. K. Lee, M. J. Sandoval and A. T. Bell, *J. Catal.*, 1994, **150**, 81–93.
- 64 S. Kattel, B. Yan, Y. Yang, J. G. Chen and P. Liu, *J. Am. Chem. Soc.*, 2016, **138**, 12440–12450.
- 65 D. B. Clarke and A. T. Bell, *J. Catal.*, 1995, **154**, 314–328.
- 66 M. A. Bañares, L. J. Alemany, M. L. Granados, M. Faraldos and J. L. G. Fierro, *Catal. Today*, 1997, **33**, 73–83.
- 67 R. Klein, M. D. Scheer and L. J. Schoen, *J. Am. Chem. Soc.*, 1956, **78**, 50–52.